AGU PUBLICATIONS

Water Resources Research

RESEARCH ARTICLE
10.1002/2015WR017290

Key Points:
- Dimensionally reduced equations for multiphase flow and poroelasticity
- Efficient and accurate hydromechanical analysis of high aspect ratio aquifers
- Vertical Equilibrium and Linear Vertical Deflection assumptions in dimensionally reduced models

Correspondence to:
T. I. Bjørnarå,
tore.ingvald.bjornara@ngi.no

Citation:
Bjørnarå, T. I., J. M. Nordbotten, and J. Park (2016), Vertically integrated models for coupled two-phase flow and geomechanics in porous media, *Water Resour. Res.*, *52*, 1398–1417, doi:10.1002/2015WR017290.

Received 24 MAR 2015
Accepted 30 JAN 2016
Accepted article online 5 FEB 2016
Published online 28 FEB 2016

Vertically integrated models for coupled two-phase flow and geomechanics in porous media

Tore I. Bjørnarå[1,2], Jan M. Nordbotten[1], and Joonsang Park[2]

[1]Department of Mathematics, University of Bergen, Bergen, Norway, [2]NGI, Oslo, Norway

Abstract Models of reduced dimensionality have been found to be particularly attractive in simulating the fate of injected CO_2 in supercritical state in the context of carbon capture and storage. This is motivated by the confluence of three aspects: the strong buoyant segregation of the lighter CO_2 phase above water, the relatively long time scales associated with storage, and finally the large aspect ratios that characterize the geometry of typical storage aquifers. However, to date, these models have been confined to considering only the flow problem, as the coupling between reduced dimensionality models for flow and models for geomechanical response has previously not been developed. Herein, we develop a fully coupled, reduced dimension, model for multiphase flow and geomechanics. It is characterized by the aquifer(s) being of lower dimension(s), while the surrounding overburden and underburden being of full dimension. The model allows for general constitutive functions for fluid flow (relative permeability and capillary pressure) and uses the standard Biot coupling between the flow and mechanical equations. The coupled model retains all the simplicities of reduced-dimensional models for flow, including less stiff nonlinear systems of equations (since the upscaled constitutive functions are closer to linear), longer time steps (since the high grid resolution in the vertical direction can be avoided), and less degrees of freedom. We illustrate the applicability of the new coupled model through both a validation study and a practical computational example.

1. Introduction

The coupling of flow and deformation of geological porous media is important in a range of applications such as groundwater withdrawal, geothermal energy extraction, shale gas extraction, and CO_2 storage. The two latter applications require attention to multiphase flow, while all examples (perhaps with the exception of groundwater extraction) include features of high aspect ratios. These may take the form of fractures (in the case of geothermal energy or shale gas extraction) or the presence of relatively thin storage units in the case of CO_2 storage [*Celia and Nordbotten*, 2009]. Our attention is therefore drawn to modeling and simulation of multiphase flow in deformable porous media with high aspect ratios.

The combined presence of multiphase flow and thin storage layers for CO_2 storage makes models of reduced complexity attractive for large-scale simulation [*Lake*, 1989; *Nordbotten and Celia*, 2012]. This has led to the development of both simple immiscible two-phase flow models [*Hesse et al*., 2008; *Nordbotten et al*., 2005] and more elaborate models including both explicit consideration of capillary forces and hysteresis [*Nordbotten and Dahle*, 2011], partially soluble fluids with upscaled convective mixing [*Gasda et al*., 2011], as well as models including careful treatment of effective fluid properties such as spatially varying fluid density [*Andersen et al*., 2014]. Such upscaled, or vertically integrated, models, have been applied to assess real field data [*Celia et al*., 2011; *Mykkeltvedt and Nordbotten*, 2012; *Nilsen et al*., 2011] and participated in benchmark studies [*Class et al*., 2009; *Nordbotten et al*., 2012], while their range of validity has been established by several authors both numerically [see e.g., *Court et al*., 2012] and analytically [see e.g., *Yortsos*, 1995].

Reduced models for coupled flow and mechanics have received comparatively less attention, with little work appearing after the early work of Bear and Corapcioglu [*Bear and Corapcioglu*, 1981a,b; *Corapcioglu and Bear*, 1983]. In particular, no work has shown how to couple the vertically integrated multiphase flow models of the previous paragraph to mechanical deformation.

In this work, we show the first complete model including a consistent, vertically integrated approach for coupled multiphase flow and mechanical deformation. We consider the setting of thin porous layers, such

as aquifers, embedded in a larger physical domain (typically denoted overburden and underburden). Our interest is thus in the case where the thin layer can be upscaled to a lower dimensional surface, on which vertically integrated equations govern the physics, while we will retain the full-dimensional formulation outside the thin layer.

Throughout this paper, we consider the context of CO_2 storage, wherein CO_2 in supercritical state is injected into an underground geological formation, e.g., a saline aquifer or an abandoned oil or gas reservoir [*Celia et al*., 2015]. Our interest herein is safe storage, and in particular the mechanical integrity of the reservoir and overlying caprock. In this context, hydromechanical models are essential in order to evaluate induced stresses with respect to failure envelopes or strengths of reservoir and surrounding seals. These models describe the interaction between the porous media and the fluid, linking the stress and the pore pressure. We consider this coupling within the theory of poroelasticity. A general description of this theory was first considered by *Biot* [1935] and his later works [*Biot*, 1941, 1955, 1972, 1973], and later this initial work has been given a more rigorous theoretical foundation [see for instance *Rice and Cleary*, 1976; *Ferrín and Mikelić*, 2003; E. Detournay and A. H.-D. Cheng, Fundamentals of poroelasticity, unpublished data, 1993].

There is an extensive literature on the subject of hydromechanical coupling. More particularly, in relation to CO_2 storage, the industrial-scale projects have been subject to numerous modeling studies. At the Sleipner CO_2 storage site off the shore of Norway, flow analysis has been the main focus due to the excellent injectivity, large storage capacity, and the availability of 4-D seismic that images the extent of the injected CO_2 plume. However, at the In Salah storage site in Algeria, the unusual upheaval patterns at the surface that was detected by satellite surveys (InSAR), particularly around one of the three injection wells, attracted much attention to the hydromechanical coupling. Indeed, early studies suggested the presence of a high-permeable fault system intersecting one of the injection wells [*Vasco et al*., 2008] which was also later confirmed by updated seismic (in 2009) [*Ringrose et al*., 2013] and further supported by several additional modeling studies [e.g., *Durucan et al*., 2011; *Gemmer et al*., 2012; *Rinaldi and Rutqvist*, 2013; *Rutqvist et al*., 2010; *Shi et al*., 2012]. The thermohydromechanical coupling at In Salah has been studied by *Preisig and Prévost* [2011] and *Gor et al*. [2013], suggesting that nonisothermal effects and thermal stress can be important to consider when evaluating the integrity of a CO_2 storage site, particularly when significant temperature variations are expected. Despite this, the isothermal approximation is a common simplification in the context of CO_2 storage modeling. Most often isenthalpic conditions are assumed, implying that temperature conditions are considered in determining the material properties, but heat transport due to fluid flow is not.

Our emphasis throughout this manuscript therefore lies on the context of vertically integrated hydromechanical models, and in particular the novel treatment of mechanical deformation, which we term Linear Vertical Deflection (LVD). The LVD equations are the dimensionally reduced (integrated) equations for linear elasticity. We see this model in the broader setting of a hierarchy of models with different complexity [*Celia and Nordbotten*, 2009]. Such a hierarchy is particularly valuable, as the different stages of operation (screening, ranking, planning, and operation) have very different data availability and computational objectives. As such, it is both infeasible and undesirable to make a full 3-D simulation in the screening stage of operations, and at this stage, simplified models have particular value. At the same time, we point out that fully resolved 3-D simulations may be computationally infeasible even for relatively simple problems in the presence of coupled processes, as was emphasized both in a recent benchmark study [*Nordbotten et al*., 2012], and in subsequent work [*Elenius et al*., 2015].

We structure the rest of this manuscript as follows: in section 2, we give a brief review of hydromechanical coupling in the context of CO_2 storage. In section 3, we derive the vertically integrated model of interest herein. To demonstrate the applicability of the method, we consider a prototypical storage simulation, which is presented in section 4 and analyzed numerically in section 5. We conclude the paper in section 6.

2. Governing Equations

The basic concepts of poroelastic behavior can be divided into primary and secondary coupling [*Rutqvist and Stephansson*, 2003; *Wang*, 2000]. The primary coupling occurs through deformation and pore fluid interactions and relates to changes in the pore volume and the volumetric strain rate. A change in stress produces a change in fluid pressure or fluid mass (solid-to-fluid coupling) and a change in the pore fluid pressure or fluid mass produces a change in the volume of the porous material (fluid-to-solid coupling). The

secondary coupling considers indirect effects where a change in the stress causes a change in the hydraulic properties of the rock mass (solid-to-fluid) and a change in the pore fluid pressure causes a change in the mechanical properties of the rock mass (fluid-to-solid). Herein, we will for simplicity of exposition consider only the primary coupling; however, the results extend also to the secondary coupling phenomena.

In the following, we give the relevant components of the theory of the multiphase extension of Biot's theory. While the equations for fluid flow and mechanical deformation are coupled, it is natural to present them separately. Throughout this section, we will consider only small deformations, and the coordinate system is Lagrangian with respect to the solid.

2.1. Fluid Flow Equations

For notational simplicity, to focus on the problem of coupling vertical equilibrium two-phase flow models with larger geomechanical models, some simplifying assumptions will be made. First, only two phases will be considered: wetting and nonwetting phase. The wetting phase is the resident aqueous phase which is assumed to mainly consist of water, and the nonwetting phase is CO_2 in a supercritical state due to the pressure and temperature conditions (approximately 90°C and 18–19 MPa, see e.g., *Morris et al*. [2011], *Preisig and Prévost* [2011], and *Deflandre et al*. [2011], compared to the critical point of CO_2 at 31°C and 7.4 MPa [*Lide*, 2003]). Second, mutual dissolution of the phases is ignored. For a temperature range of 50°C–100°C, a pressure range of 10–30 MPa, and high salinity (formation water is typically saline), the volume fraction of CO_2 that can dissolve in brine and the volume fraction of brine that can dissolve in CO_2 is typically in the order of 0.06 and 0.003, respectively [*Yan et al*., 2011]. Miscibility can be an important effect to consider when evaluating long-term CO_2 storage efficiency, but this has previously been explored in the nondeformable setting, e.g., by *Gasda et al*. [2011]. Last, thermodynamic effects are ignored. When large temperature differences are expected, thermodynamic effects can be important to consider, but this has also been explored in the nondeformable setting, e.g., by *Andersen et al*. [2014]. Therefore, within the aquifer formation, the relevant governing equations for the two-phase immiscible flow system can be written as follows:

$$\frac{\partial(\phi\rho_\alpha s_\alpha)}{\partial t} = -\nabla\cdot(\rho_\alpha\phi s_\alpha \mathbf{v}_\alpha) \tag{1}$$

where ϕ is the porosity and ρ_α (kg/m^3) and s_α are the density and saturation of the fluid phase α, respectively. The phase velocity $\mathbf{v}_\alpha$ (m/s) is related to the Darcy flux $\mathbf{q}_\alpha$ (m/s) in a deforming media by the following relation:

$$\mathbf{q}_\alpha = \phi s_\alpha(\mathbf{v}_\alpha - \mathbf{v}_s) = -\frac{\mathbf{k}}{\mu_\alpha}k_{r\alpha}(\nabla p_\alpha - \rho_\alpha \mathbf{g}) \tag{2}$$

where $\mathbf{v}_s$ (m/s) is the velocity of the solid deformation, $\mathbf{k}$ (m^2) is the material permeability tensor, $\mathbf{g}$ (m/s^2) is the gravity vector and μ_α (Pa s), $k_{r\alpha}=k_{r\alpha}(s_\alpha)$, and p_α (Pa) are the dynamic viscosity, relative permeability, and fluid pressure for phase α, respectively. With the focus on CO_2 injected into a water-filled aquifer, we need only consider a nonwetting (n) and wetting phase (w), respectively, where $\alpha=n$ for the supercritical gas phase consisting mainly of CO_2 and $\alpha=w$ for the resident water. The capillary pressure, p_c (Pa), is defined by

$$p_c(s_\alpha) = p_n - p_w \tag{3}$$

Furthermore, it can be understood that since no other phases are present, the phase fractions of water and CO_2 satisfy

$$s_w + s_n = 1 \tag{4}$$

Considering the mass conservation of the solid phase:

$$\frac{\partial[\rho_s(1-\phi)]}{\partial t} + \nabla\cdot[\rho_s(1-\phi)\mathbf{v}_s] = 0 \tag{5}$$

where ρ_s (kg/m^3) is the density of the solid constituents of the porous medium. Using the equation of state for the solid, acknowledging that the density depends on the pore pressure acting on the solid, p_s (Pa), temperature T (°C), and the first invariant of the effective stress, I_1' (Pa); $\rho_s=\rho_s(p_s, T, I_1')$, the following expression for the change in porosity can be obtained, following *Lewis and Schrefler* [1998]:

$$\frac{d\phi}{dt}=(b-\phi)\left[c_s\frac{dp_s}{dt}-\beta_s\frac{dT}{dt}+\nabla\cdot\mathbf{v}_s\right] \tag{6}$$

where b is the Biot's coefficient and c_s (1/Pa) and β_s (1/K) are the compressibility and the volumetric thermal expansion coefficient for the solid phase, respectively. When assuming isothermal conditions and using equations (2), (5), and (6), equation (1) can finally be expanded to

$$\begin{aligned}\phi\rho_\alpha\frac{\partial s_\alpha}{\partial t}+\phi s_\alpha\rho_\alpha c_\alpha\frac{\partial p_\alpha}{\partial t}+\nabla\cdot(\rho_\alpha\mathbf{q}_\alpha)\\ +s_\alpha\rho_\alpha\left[(b-\phi)c_s\frac{\partial p_s}{\partial t}+b\frac{\partial\varepsilon_v}{\partial t}\right]=0\end{aligned} \tag{7}$$

where c_α (1/Pa) is the compressibility of fluid phase α obtained from the equation of state (for isothermal conditions and immiscible phases):

$$c_\alpha=\frac{1}{\rho_\alpha}\frac{\partial\rho_\alpha}{\partial p_\alpha} \tag{8}$$

and we have used that the rate of change of volumetric strain ε_v can be expressed as $\partial\varepsilon_v/\partial t=\nabla\cdot\mathbf{v}_s$.

The pore pressure, p_s, is typically defined as the sum of the saturation averaged phase pressures according to [e.g., *Bishop*, 1959; *Jaeger et al.*, 2007; *Lewis and Schrefler*, 1998]:

$$p_s=\sum_\alpha s_\alpha p_\alpha \tag{9}$$

Using the capillary pressure in equation (3), equation (9) can be rearranged to

$$p_s=p_w+s_n p_c \tag{10}$$

Under many typical reservoir conditions, the last term $s_n p_c$ is small compared to p_w, such that $p_s\approx p_w$ is often used. We note that this already suggests that the fluid-to-solid coupling will primarily be through the fluid pressures, while more weakly dependent on saturation.

2.2. Geomechanical Equations

Under quasi-static conditions, the balance of momentum leads to the equation of equilibrium. In differential form, we then obtain (assuming static initial conditions):

$$\nabla\cdot(\sigma'-b\Delta p\mathbf{I})+\Delta\mathbf{f}=0 \tag{11}$$

where σ' (Pa) is the effective stress tensor, Δp (Pa) is the change in pore pressure relative to initial, steady state pore pressure, $\mathbf{I}$ is the identity matrix, and $\Delta\mathbf{f}$ (N/m^3) is the change in volumetric bodyload vector, again, relative to steady state conditions. Note that we use a stress convention where positive stress is extensional. The effective stress σ' is defined as the part of the total stress that governs the deformation of a rock, or soil. In rocks, the Biot coefficient describes the difference between the pore volume change and the bulk volume change during hydrostatic deformation and can be defined as $b=1-K/K_s$, where K (Pa) is the dry (drained) bulk modulus of the porous media and $K_s=1/c_s$ (Pa) is the solid bulk modulus (of the solid material/mineral in the porous media).

In addition, a constitutive equation relates stresses and strains, for isotropic materials they relate linearly according to

$$\sigma'=\lambda\varepsilon_v\mathbf{I}+2G\varepsilon \tag{12}$$

where the mechanical properties are here given by the Lamé parameters λ (Pa) and G (Pa). The volumetric strain is defined as $\varepsilon_v=\nabla\cdot\mathbf{u}$, where $\mathbf{u}$ (m) is the displacement vector and the full strain tensor ε is defined as

$$\varepsilon=\frac{1}{2}\left[\nabla\mathbf{u}+(\nabla\mathbf{u})^T\right] \tag{13}$$

We note again that in this convention the stresses and strains are positive for elongation and negative for compression.

The initial vertical stress is equal to the weight of the overburden; both the porous media and the pore fluids:

$$\sigma_v(z) = p_{atm} + \int_0^z \rho g dz \tag{14}$$

$$\rho = (1-\phi)\rho_s + \phi \sum_\alpha s_\alpha \rho_\alpha \tag{15}$$

where z (m) is the vertical elevation. When modeling under the assumption of steady state initial conditions, we are only interested in the change of stress, thus from equation (15) we see that a change in saturation s_α may change the buoyancy of the pore fluid and thereby alter the vertical stress through the $\Delta\mathbf{f}$-term in equation (11).

3. Dimensionally Reduced Model

Due to the often layered nature of reservoirs, aquifers, and aquitards, the horizontal extent is often much larger than the vertical extent and we can refer to them as large aspect ratio geological features. This property allows us to justify assumptions on the local vertical structure of the solution. In this section, we exploit these ideas in order to derive approximations to the governing equations for two-phase flow and poroelasticity.

In Figure 1, a conceptual sketch of such a system is shown. An aquifer is located between an overburden and underburden and shows topographic behavior. Note that in this figure, the vertical dimension has been exaggerated severely; for geological formations considered for CO_2 storage, the maximum slopes are typically only at most a few degrees.

With reference to the figure, the bounding surfaces of the aquifer are denoted F_B and F_T, where the function for surface F_n is defined as

$$F_n(x,y,z) = z - \zeta_n(x,y) = 0 \tag{16}$$

and $\zeta_n(x,y)$ (m) is the vertical position of the surface. This notation allows us to define the normal vector $\mathbf{n}$ of surface n as

$$\mathbf{n} = \nabla F_n \tag{17}$$

Note that these normal vectors are scaled such that the vertical extent equals 1, thus the vectors satisfy $||\mathbf{n}|| \geq 1$.

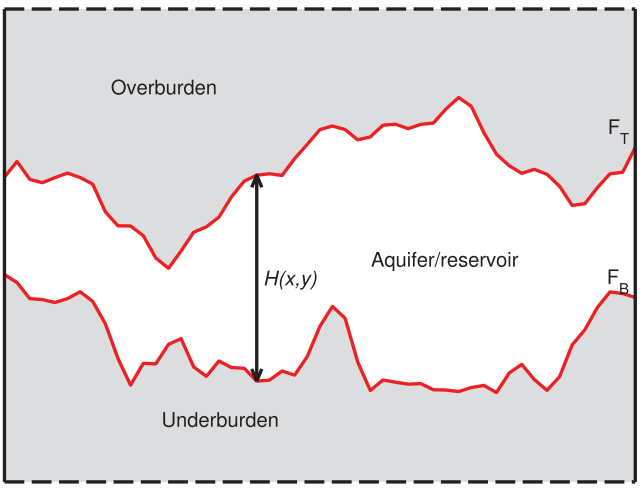

Figure 1. Example of an aquifer/reservoir of varying thickness H, located between an overburden and underburden.

In this section, we will first recall the integrated fluid flow model for immiscible two-phase flow [*Nordbotten and Dahle*, 2010; *Yortsos*, 1995], and subsequently consider the analogue model for mechanical deformation. To keep notation simple, we will not consider vertical variability in the material or fluid parameters within an aquifer. Thus, some properties will keep the same notation in both the full-dimensional formulation and the dimensionally reduced formulation.

3.1. Vertically Integrated Flow Model

We first consider the integrated form of mass conservation that will be obtained from equation (7). By assuming constant material properties in the vertical/integration direction and applying

Leibniz' rule when integrating each term in equation (7) from $z=\zeta_B$ to $z=\zeta_T$, the following dimensionally reduced form of the mass conservation for fluid phase α is obtained:

$$\begin{aligned}&\phi\rho_\alpha\frac{\partial S_\alpha}{\partial t}H+\phi S_\alpha\rho_\alpha c_\alpha\frac{\partial P_\alpha}{\partial t}H+\tilde{\nabla}\cdot(\rho_\alpha\mathbf{Q}_\alpha)\\&+S_\alpha\rho_\alpha\left((b-\phi)c_s\frac{\partial P_s}{\partial t}+b\frac{\partial E_v}{\partial t}\right)\\&+\rho_\alpha(\mathbf{q}_\alpha\cdot\mathbf{n})|_T-\rho_\alpha(\mathbf{q}_\alpha\cdot\mathbf{n})|_B=0\end{aligned}\tag{18}$$

where $H=H(x,y)$ (m) is the thickness of the aquifer and we have introduced the notation for the horizontal gradient

$$\tilde{\nabla}=\left[\frac{\partial}{\partial x},\frac{\partial}{\partial y},0\right]^T\tag{19}$$

and the integrated volumetric strain is defined as

$$E_v=\int_{\zeta_B}^{\zeta_T}\varepsilon_v dz=\int_{\zeta_B}^{\zeta_T}\nabla\cdot\mathbf{u}dz\tag{20}$$

which is discussed further in equation (30) and section 3.3.3. Recall from equation (16) that ζ_B and ζ_T are the vertical positions of the bottom and top of the aquifer, respectively. Furthermore, we have introduced the representative pressure P_α (Pa) as the fluid pressure for fluid phase α at a specified datum $z=\zeta_P$; $P_\alpha=p_\alpha(x,y,\zeta_P,t)$. From the assumptions of constant density in the vertical direction, the fluid phase pressure can be expressed as

$$p_\alpha(x,y,z,t)=P_\alpha(x,y,t)-\rho_\alpha g[z-\zeta_P(x,y)]\tag{21}$$

Thus, we have for the integrated pore pressure:

$$P_s=\int_{\zeta_B}^{\zeta_T}\sum_\alpha\hat{s}_\alpha[P_\alpha-\rho_\alpha g(z-\zeta_P)]dz\tag{22}$$

where the datum ζ_P is typically chosen as the top or bottom surface of the aquifer and the integrated Darcy flux and average saturation S_α of phase α can be expressed as

$$\mathbf{Q}_\alpha=\int_{\zeta_B}^{\zeta_T}\mathbf{q}_\alpha dz\tag{23}$$

$$S_\alpha=\frac{1}{H}\int_{\zeta_B}^{\zeta_T}\hat{s}_\alpha dz\tag{24}$$

We will return to how to obtain explicit expressions for the integrated flux $\mathbf{Q}_\alpha$ and the reconstructed inverted capillary saturation $\hat{s}_\alpha$ in section 3.3 on closure relationships. Terms including the normal vector $\mathbf{n}$ in equation (18) represent the mass flux of fluid phase α across the top and bottom boundaries of the aquifer and are derived directly from the integration of the divergence term in equation (7) upon applying the Leibniz' rule.

3.2. Integrated Deflection Model

In the context of regional land subsidence due to ground water pumping, a series of papers on regional scale vertically averaged models for deformation were developed by Bear and Corapcioglu in 1981 and 1983 [*Bear and Corapcioglu*, 1981a,b; *Corapcioglu and Bear*, 1983]. There they developed a mathematical model for the areal distribution of drawdown, land subsidence, and horizontal displacement. The horizontal two-dimensional model was derived by averaging the three-dimensional model over the vertical thickness of the aquifer and taking into account the continuous variation in total stress as a result of water table fluctuations. The total stress is due to water and soil overburden weight and the vertical compaction and horizontal displacement is assumed to occur only in the reservoir where the pore pressure changes. In reality, most often the poroelastic effect extends far beyond the reservoir. For instance, the displacements will attenuate in the vertical direction as the pore pressure change also dissipates into the overburden and

underburden. This earlier work further assumed that the horizontal displacement was constant across the thickness of the aquifer and the vertical displacement varied linearly across the thickness of the reservoir.

Herein, we deviate from earlier work by treating the reservoir as an embedded region in a full three-dimensional domain, thus accounting fully for the full stress tensor in the overburden and underburden. Furthermore, we extend the fluid description to allow for multiple phases, here two phases, and consider linearly varying displacement across the thickness of the aquifer in both the horizontal and the vertical direction. Also considering linearly varying horizontal displacement across the aquifer thickness can be particularly important when noncorrelated displacement at the top and bottom of the aquifer is expected, for instance when the reservoir of interest shows topographical behavior, is inclined and/or the surrounding formations exhibit significant contrasts in mechanical properties. The effect of topography is illustrated and discussed further in section 5.3.

To obtain the compatible momentum balance equation to the VE formulations for two-phase flow, the equilibrium equation in equation (11) is integrated across the thickness of the aquifer in the vertical z direction between two surfaces F_B and F_T to obtain (in analogy to equation (18)):

$$\tilde{\nabla}\cdot\Sigma+(\sigma\cdot\mathbf{n})|_T-(\sigma\cdot\mathbf{n})|_B=\Delta\mathbf{F} \tag{25}$$

where we have introduced the integrated stress

$$\Sigma=\int_{\zeta_B}^{\zeta_T}\sigma dz \tag{26}$$

and the change in the integrated bodyload vector, $\Delta\mathbf{F}$. We recall that the total stress σ can be expressed as

$$\sigma=\lambda(\nabla\cdot\mathbf{u})\mathbf{I}+\mu\left(\nabla\mathbf{u}+(\nabla\mathbf{u})^T\right)-b\Delta p\mathbf{I} \tag{27}$$

Thus, the integral in equation (26) can be evaluated by inserting equation (27) and using Leibniz' integral rule, to obtain:

$$\begin{aligned}\Sigma=&\lambda\left[\tilde{\nabla}\cdot\mathbf{U}\right]\mathbf{I}+\mu\left[\tilde{\nabla}\mathbf{U}+(\tilde{\nabla}\mathbf{U})^T\right]-b\Delta P_s\mathbf{I}\\&+\lambda(\mathbf{u}\cdot\mathbf{n}|_T-\mathbf{u}\cdot\mathbf{n}|_B)\mathbf{I}\\&+\mu(\mathbf{nu}|_T-\mathbf{nu}|_B)\\&+\mu(\mathbf{un}|_T-\mathbf{un}|_B)\end{aligned} \tag{28}$$

where we have introduced the integrated displacement vector

$$\mathbf{U}=\int_{\zeta_B}^{\zeta_T}\mathbf{u}dz \tag{29}$$

and have that the volumetric strain E_v in equation (20) can now be expressed as

$$E_v=\tilde{\nabla}\cdot\mathbf{U}+(\mathbf{u}\cdot\mathbf{n})|_T-(\mathbf{u}\cdot\mathbf{n})|_B \tag{30}$$

Together, equations (25) and (28) form the governing Poroelastic Linear Vertical Deflection (PLVD) equations for the geomechanical system. The PLVD equations are thus the dimensionally reduced (integrated) equations of equilibrium for a poroelastic medium. How to obtain the explicit expression for the integrated displacement in equation (29) is described in section 3.3.3.

3.3. Closure Relationships

In order to complete the description of the vertically integrated model, it is necessary to make modeling assumptions regarding the structure of the solution within the aquifer [*Nordbotten and Celia*, 2012]. Specifically, this is required in order to obtain explicit expressions for $\mathbf{Q}_\alpha$ and to relate P_α and $\mathbf{U}$ to the values at the top and bottom of the aquifer.

Two main categories of closure relationships can be postulated for the main variables: (A) The internal structure is in a certain sense constant across the thickness of the aquifer. (B) The internal structure varies linearly across the thickness of the aquifer.

3.3.1. Pressure

It is common for the fluid equations to use closure form (A), wherein the fluid potential (pressure and hydrostatic effects; $p_\alpha + \rho_\alpha g z$) is assumed to be vertically uniform within the aquifer. In order to be consistent with previous studies, we will adopt this convention here. This implies that the fluid pressures are close to being in vertical equilibrium, and thus the vertical gradients are proportional to the specific gravity of the fluid. The term VE model refers to models where this assumption is applied. For each phase, the hydrostatic fluid pressure can thus be expressed by equation (21), this is schematically illustrated for the wetting phase pressure for $\zeta_P = \zeta_B$ in Figure 2.

When significant fluid flow occurs through the aquifer, the approximation of constant vertical potential may be questioned [*Guo et al*., 2014; *Nordbotten and Celia*, 2006]. However, due to the permeability contrast between the aquifer and overburden, the dominant vertical variation in fluid potential is within the overburden and underburden [*Hunt*, 1985]. The use of constant fluid potential within the aquifer has the modeling advantage that the saturation reconstruction equation in Appendix A, equation (A1), does not depend on vertical flux.

3.3.2. Saturation and Flux

The choice of constant fluid potential across the aquifer thickness allows us to exploit the capillary pressure curve to derive the nonlinear structure of the variable $\hat{s}_\alpha$ as a function of the vertical elevation z [*Nordbotten and Dahle*, 2010]. When ignoring hysteresis in the capillary pressure function, the saturation can be solved for by inverting equation (3) such that $s_\alpha = p_c^{-1}(p_n - p_w)$, thus, since the capillary pressure is in vertical equilibrium, the saturation also becomes a distribution over the vertical elevation; $\hat{s}_\alpha = p_c^{-1}(z)$, see Figure 3. We detail an explicit expression on this form in Appendix A. Together with the definition of the fluid flux, we can then derive explicit expressions for the integrated flux in the form:

$$\mathbf{Q}_\alpha = -\frac{\mathbf{k}\Lambda_\alpha H}{\mu_\alpha}(\nabla P_\alpha - \rho_\alpha G) \tag{31}$$

where G (m/s^2) is the gravity contribution in the horizontal direction due to the topography of the datum ζ_P.

The average fluid mobility term is defined as

$$\Lambda_\alpha \equiv \frac{1}{H}\int_{\zeta_B}^{\zeta_T} \lambda_\alpha(\hat{s}_\alpha)\,dz \tag{32}$$

where $\lambda_\alpha(\hat{s}_\alpha)$ is a function of the reconstructed inverted capillary saturation. Explicit expressions for Λ_α when λ_α can be expressed by Corey-type power law functions, e.g., equations (38) and (39), can be obtained from equations (A2) and (A3), respectively.

Note that when the capillary pressure is ignored, the mobility simplifies and is directly proportional to the saturation [see e.g., *Nordbotten and Celia*, 2012, chapter 3.7; *Nordbotten and Dahle*, 2010].

3.3.3. Displacement

It is important to note that it is not sufficient to use an assumption of constant vertical displacement across the aquifer thickness for our application, since the vertical expansion of the aquifer itself is an important feature of the solution. In addition, for aquifers with general topography, the overburden and underburden may have noncorrelated displacement, and standard reduced models with constant horizontal displacement may be qualitatively wrong. Thus, we are led to consider a closure relationship in the form (B). The term LVD (Linear Vertical Deflection) for the dimensionally

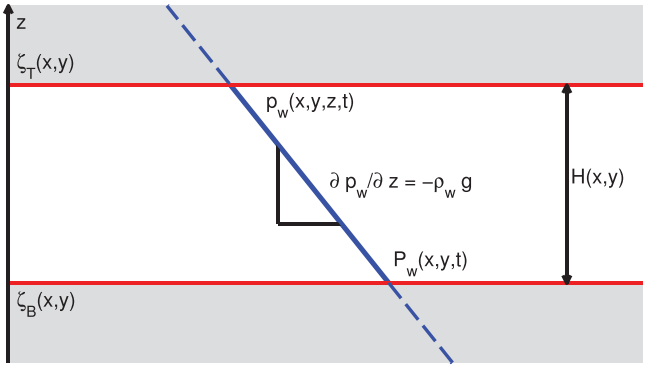

Figure 2. Vertical equilibrium pressure profile for the wetting phase (blue line). The white area represents the aquifer and the red lines are the upper and lower bounds of the aquifer. The dashed blue lines indicate continuity in wetting phase pressure into the overburden and underburden.

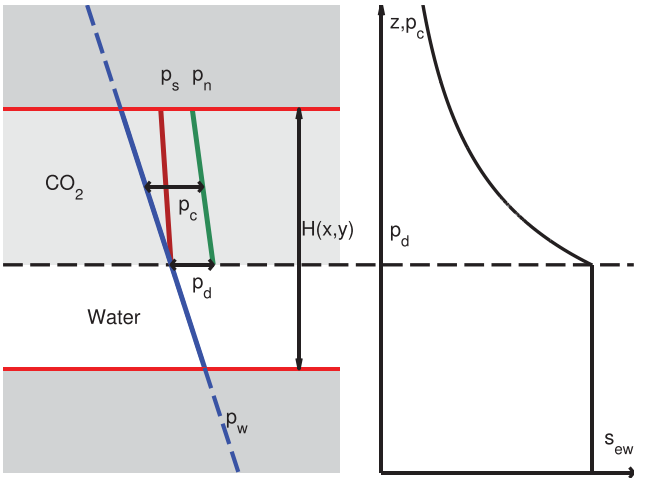

Figure 3. Schematic comparison of the phase pressure and pore pressure profiles across an aquifer in vertical equilibrium with the capillary pressure function. p_d (Pa) is the entry pressure in the capillary pressure function. The horizontal dashed line indicates where effective nonwetting saturation $s_{en} = 0$ and the light grey area indicates the two-phase flow region. Here the aquifer is assumed to be confining for the nonwetting phase and the dashed blue lines indicate the continuity in the wetting phase pressure.

reduced form of the equation of equilibrium and its poroelastic extension, PLVD (Poroelastic Linear Vertical Deflection), have already been introduced. The names reflect the assumed structure of the displacement vector **u** which varies linearly in the vertical direction across the thickness of the aquifer according to

$$\mathbf{u} = \mathbf{u}_B + \frac{\mathbf{u}_T - \mathbf{u}_B}{H}(z - \zeta_B) \tag{33}$$

where the subscripts T and B indicate top and bottom of the aquifer, respectively. The integrated displacement in equation (29) can now be evaluated to

$$\mathbf{U} = \frac{\mathbf{u}|_T + \mathbf{u}|_B}{2} H \tag{34}$$

This is, however, not sufficient to form a closed system of equations, and we need to complement equation (34) with a consistency requirement on the vertical stresses. From equation (28), we know that the vertical component of integrated stress is given by Hooke's law and the displacement at the top and bottom of the aquifer. Furthermore, we require that this integrated stress is compatible with the stress at the aquifer top and bottom, e.g.,

$$\boldsymbol{\Sigma} \cdot (\mathbf{n}|_T + \mathbf{n}|_B) = [(\sigma \cdot \mathbf{n})|_T + (\sigma \cdot \mathbf{n})|_B]H \tag{35}$$

3.4. Comments on Generality

In the preceding sections, we have consciously suppressed several nuances in the interest of obtaining a relatively concise presentation. We note a few of them here.

Saturation within an aquifer. We have suppressed to some extent explicit notation regarding the vertical structure of saturation [*Nordbotten and Celia*, 2012]. It is implied in all vertically integrated flow models that the saturation structure can be reconstructed from the integrated saturation, and we have denoted this reconstructed saturation, where needed, as $\hat{s}_\alpha$. Note that this reconstructed saturation can be obtained analytically or numerically; however, these nuances have been explored in earlier work [*Doster et al*., 2013].

Shape of pressure profile. In the preceding, we have in the interest of being compatible with the majority of earlier work on vertically integrated flow models used the convention from vertically integrated models wherein the vertical distribution of pressure is hydrostatic. However, it is possible to use also for the flow equation a nonhydrostatic vertical distribution, although this has received less attention [*Nordbotten and Celia*, 2006].

Assumptions on physical parameters. The general integrated conservation equations (18) and (25) are valid without regard to any assumptions on parameters. It is also possible to derive the constitutive laws in equations (28) and (31) with greater generality; however, this typically comes at the price of significant added complexity in the definitions of the effective parameters for the integrated equations [*Andersen et al*., 2014; *Nordbotten and Celia*, 2012].

4. Validation Model

The validation model is inspired by the study on CO_2 injection and ground deformations at In Salah, Algeria, by *Rutqvist et al*. [2010]. In this example, CO_2 is injected into a 20 m thick, flat, and horizontal reservoir with a 900 m thick caprock layer, see Figure 4. The hydromechanical material properties are given in Table 1. The pressure and temperature conditions at reservoir level (approximately 90°C and 18–19 MPa) imply that the CO_2 is in supercritical state and the fluid properties that are used are given in Table 2. In the present paper,

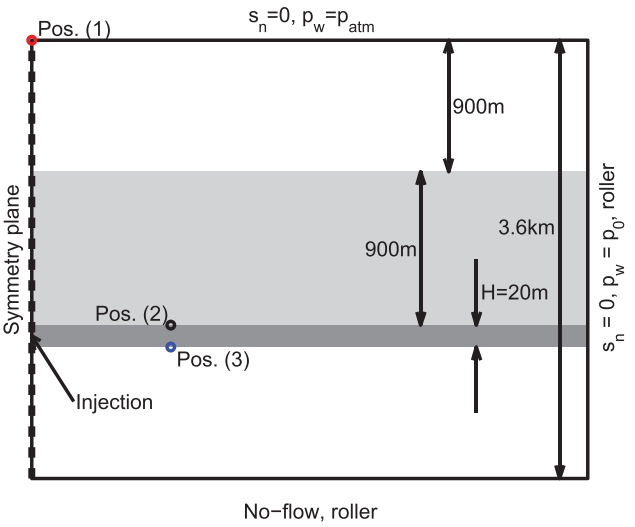

Figure 4. Sketch of model geometry of validation model and boundary conditions. Position (1)–(3) indicate the location where the values in the convergence plot in Figure 13 are obtained. Positions (2) and (3) are located at top and bottom of the aquifer, respectively, at $x = 500$ m. Initial pressure p_0 is hydrostatic with a constant vertical gradient and the pores are initially fully water saturated, $s_n = 0$.

we choose to work with dimensional variables, due to the large number of parameters associated with defining poroelastic formulations in the geometric setting of multilayered geological materials. For this problem, there is no clearly preferred choice of characteristic scales, and we find that using a nondimensional formulation for this problem would give an undue emphasis to the somewhat arbitrary choice of scaling.

It is assumed that initially the pores are fully water saturated and the initial pore pressure p_0 (Pa) is hydrostatic with atmospheric pressure at the surface, see Figure 4. The right boundary is defined as an open boundary where the pressure is equal to the initial pressure, the bottom is a no-flow boundary and the left boundary has symmetry conditions.

The aquifer is considered partially leaky where the injected CO_2 is confined to the aquifer. The water, however, is allowed to escape/enter the aquifer and we have a continuity in both the wetting phase flux and pressure across the interface between top and bottom of the aquifer and the caprock and underburden, respectively: $q_{w,u}=q_{w,d}$ and $p_{w,u}=p_{w,d}$ [*Helmig*, 1997], where u and d indicate upside and downside of both the top and bottom aquifer boundaries, respectively.

The numerical implementation was within the framework of the commercially available software COMSOL Multiphysics, which utilizes finite elements and standard linear and nonlinear solvers.

The validation model is two-dimensional, under plane strain conditions. Note that although the equations, as presented and derived in sections 2 and 3, are applicable to three-dimensional problems, a two-dimensional validation model is chosen for greater flexibility in terms of assessing computational performance. The validation model is also consistent with an approximation to a horizontal well, such as was in use at In Salah, and here the injection is at constant rate equivalent to a total yearly sequestration of 0.133 Mt of CO_2 through a horizontal, 1.5 km long injection well perpendicular to the model plane. The horizontal injection well therefore reduces to a point in the validation model and is located in the middle of the aquifer on the axial symmetry line at $x = 0$.

4.1. Capillary Pressure and Relative Permeability Functions

The capillary pressure is described by a Brooks and Corey-type function:

$$p_c(s_n)=\alpha(1-s_{en})^{-1/2}+\beta \tag{36}$$

Table 1. Hydromechanical Material Properties Used in Validation Model

Material Property	Overburden (0–900 m)	Caprock (900–1800 m)	Reservoir (1800–1820 m)	Underburden (Below 1820 m)
Young's modulus, E (GPa)	1.5	20	6	20
Poisson's ratio, ν	0.2	0.15	0.2	0.15
Biot's coefficient, b	0.7	0.7	0.7	0.7
Porosity, ϕ	0.1	0.01	0.17	0.01
Entry pressure, γ (kPa)	NA	NA	90	NA
Permeability, k (m^2)	10^{-17}	10^{-19}	13×10^{-15}	10^{-19}
Residual saturation, wetting phase, s_{rw}	NA	NA	0.4	NA
Residual saturation, non-wetting phase, s_{rn}	NA	NA	0	NA

Table 2. Properties of Water and CO_2, Evaluated at 50°C and 20 MPa [*Linstrom and Mallard*, 2015]

	Density, ρ_α (kg/m^3)	Viscosity, μ_α (mPa s)	Compressibility, c_α (1/GPa)
Water	997	0.55	0.419
CO_2	784	0.069	15.6

where it can be seen that $\gamma \equiv \alpha+\beta$ corresponds to the entry pressure p_d (Pa) in the capillary pressure function given by *Brooks and Corey* [1964] and we use that $\gamma = 90$ kPa, $\alpha=0.9\gamma$, and $\beta=0.1\gamma$. For an initial water saturated porous medium, and since there is no residual nonwetting saturation, the effective saturation s_{en} is related to the saturation s_n by

$$s_{en} = \frac{s_n}{1-s_{rw}} \tag{37}$$

where s_{rw} is the residual wetting saturation. The relative permeability functions are given as Corey-type power law functions:

$$\lambda_n(s_n) = s_{en}^p \tag{38}$$

$$\lambda_w(s_n) = (1-s_{en})^q \tag{39}$$

where the exponents p and q are fitting parameters, here $p = 2$ and $q = 3$.

5. Results and Discussion

A two-dimensional, fully resolved poroelastic model with two-phase flow, including capillary pressure, under plane strain assumption is compared to the equivalent dimensionally reduced model using Vertical Equilibrium (VE) assumption to describe the two-phase flow in the aquifer and Poroelastic Linear Vertical Deflection (PLVD) equation to describe the poroelastic behavior in the aquifer.

As CO_2 is injected into the aquifer, the water is displaced and the pore pressure increases, resulting in increased effective stress (remembering that stress is here positive in extension) and in turn causing the formation to deform. Figure 5 shows an exaggerated deformation plot of the model, except the aquifer, where the filled contours represent the vertical displacement and the values indicate the magnitude in centimeters. The solution is taken from the fully resolved model and the black contours show the corresponding solution from the dimensionally reduced model. The white space is the aquifer and is not plotted to emphasize its expansion as the CO_2 is injected.

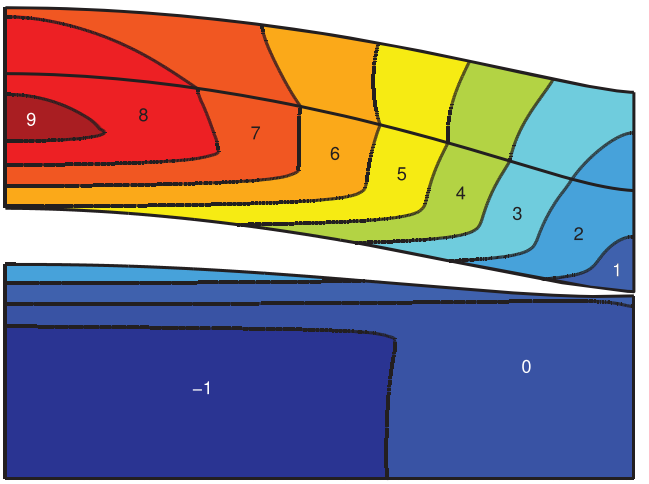

Figure 5. Exaggerated (20,000 times) deformation plot of the displacement of the overburden, caprock, and underburden after 40 years of injection. The filled contours represent the vertical displacement and the values give the vertical displacement in centimeters. The white space is the aquifer and emphasizes its expansion as the CO_2 is injected. The deformation and the colors are from the solution of the fully resolved model and the black contours are the corresponding solution from the dimensionally reduced model.

In the aquifer, the dimensionally reduced model assumes that the fluid phases are in vertical equilibrium such that the vertical flux is negligible compared to the horizontal flux. At early times, this is not a valid assumption, as is well illustrated in Figure 6 (top left) where the injected CO_2 spreads in all directions. As time progresses, the assumption becomes increasingly more appropriate and the saturation distributions of the two solutions coincide.

The main driving force for deformation is the change in stress, see equation (27). The stress depends on the pore pressure and despite the differences in the phase distribution at early time, see Figure 6, the pressure is little affected by this assumption. When comparing the injection pressure (taken as the pore pressure in the middle of the

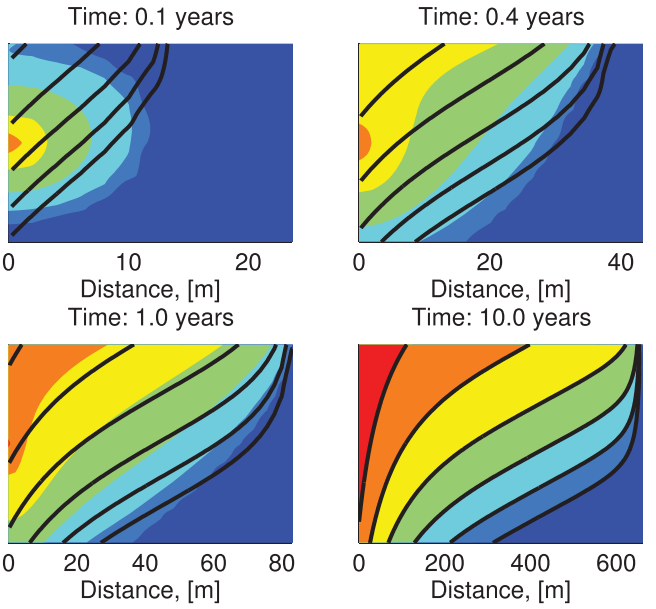

Figure 6. Saturation distribution of the CO_2 in the aquifer at various times. The filled contours are evenly distributed saturation levels ranging from 0 to 0.41. The black contours represent the corresponding distribution from the dimensionally reduced model. Note the difference in scale.

aquifer), Figure 7, it can be seen that even at early times the pressure profiles match within a small fraction. To emphasize any difference in the pressure profile, the time scale is logarithmic and the inserted axis shows the relative difference.

This weak dependency on the saturation can be explained by considering the value of the pore pressure. The initial pore pressure is approximately 18 MPa in the aquifer. For typical values of nonwetting saturation, the second term in equation (10), $s_n p_c$, becomes in the order of 0.1 MPa. Hence, it can be seen from equation (10) that $p_s \approx p_w$ and the saturation has negligible impact on the pore pressure.

The change in wetting phase pressure p_w is illustrated in Figure 8 along vertical cross sections 100 m away from the injection point. It shows how the pressure gradually dissipates out of the aquifer despite the low permeability in the caprock and underburden compared to the aquifer, and the thick dashed lines are the solution from the fully resolved model and the thin lines are from the dimensionally reduced model. The numbers indicate the time in years. Similar characteristics can be seen when looking at the change in horizontal stress σ_x, see Figure 9.

Initially, the pressure increases mainly in the aquifer, causing it to expand in all directions, and in Figure 10, it can be seen how the top and bottom of the aquifer (green and red lines, respectively) is forced apart at early times. With time, the pressure dissipates into the caprock and underburden, increasing the effective stress also here, leading eventually to the whole aquifer to heave as the underburden expands.

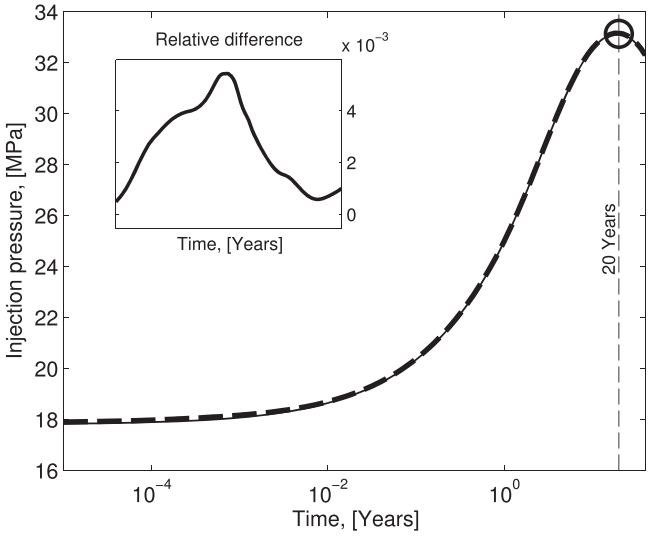

Figure 7. Evolution of the injection pressure (pore pressure in the middle of the aquifer at $x = 0$) plotted on a logarithmic time scale. Thick dashed line is the pore pressure p_s from the fully resolve model and the thin line is the pore pressure P_s from the dimensionally reduced model. The inserted axis shows the relative difference, $(p_s - P_s)/p_s$.

After 20 years of injection, the pore pressure in the aquifer reaches a maximum value, see Figure 7 and 8, but the pore pressure in the caprock and underburden continue to rise as it dissipates out of the aquifer, causing the surface to continue heaving although the aquifer has stopped expanding.

5.1. Performance and Applicability

There are two computational benefits of using a dimensionally reduced approach. First, the reduction in computational cost, which is directly related to the number of degrees of freedom that needs to be solved. Due to the two-phase flow in the aquifer, a high grid resolution may be required to resolve the distribution of phases, but in the dimensionally

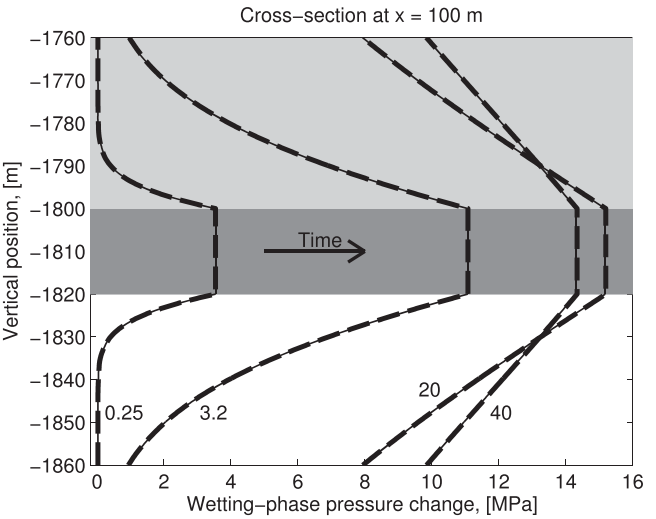

Figure 8. Vertical cross sections of the change in wetting phase pressure p_w at 100 m away from the injection point. Thick dashed lines are the solution from the fully resolved model and the thin lines are from the dimensionally reduced model. The numbers indicate the time in years.

reduced approach, the degrees of freedom inside the aquifer is eliminated altogether and the internal processes, in the aquifer, can be evaluated exactly from the upscaled variables. Second, the pressure field in flow problems is usually smooth with relatively small gradients, but two-phase and multiphase flow problems introduce volume fractions of the phases (saturation), and, depending on the hydraulic properties and the injection rate, the spatial gradients of the saturation can be very large (steeply varying saturation profile). In fact, the more convectively dominant the flow is, the steeper these gradients become. However, the dimensionally reduced model solves for the integrated mass thus the transition between the phases will be smoother and the gradients will be smaller, allowing longer time steps by the numerical solver and therefore reduced calculation time.

As indicated, in order to get physically accurate and sometimes even meaningful solutions, a numerical model usually requires a denser discretization in the two-phase flow region, and at the phase front in particular, compared to the single-phase flow region. The two-phase region is the area, or volume, where two phases are expected to sweep across in the time frame of the model. Normally, these regions are discretized differently, as illustrated in Figure 11. In the dimensionally reduced model, the two-phase flow and poroelasticity are described in the red nodes only. Hence, the reduction in computational cost is the number of degrees of freedom that can be eliminated inside the aquifer. How big this saving will be depends on the size of the two-phase region of interest.

As CO_2 displaces water, the size of the two-phase flow region will increase with times, as shown in Figure 6. To evaluate this, a study of a progressively larger two-phase flow region, allowing an increasing number of degrees of freedom to be eliminated, has been performed: eight simulations where the numerical grid in the two-phase region is dense, as in Figure 11 (left), and then gradually increase in size in the single-phase region until it looks closer to Figure 11 (right). The simulations were stopped when the CO_2 approached the extent of the more densely meshed two-phase region.

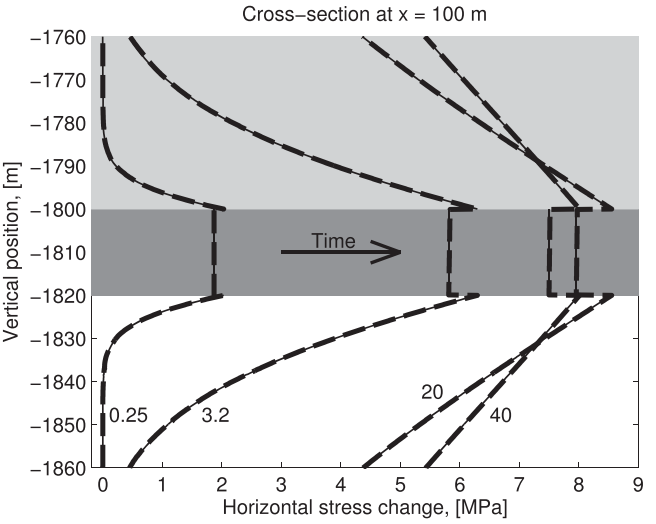

Figure 9. Vertical cross sections of the change in horizontal stress σ_x at 100 m away from the injection point. Thick dashed lines are the solution from the fully resolved model and the thin lines are from the dimensionally reduced model. The numbers indicate the time in years.

The ratio of the degrees of freedom solved for by the two models is plotted in Figure 12 (left, red line). At short times, the two-phase flow area is very small and the reduction in computational cost, by eliminating the degrees of freedom in the aquifer, is low, see for example point A in Figure 12. At longer times, the number of degrees

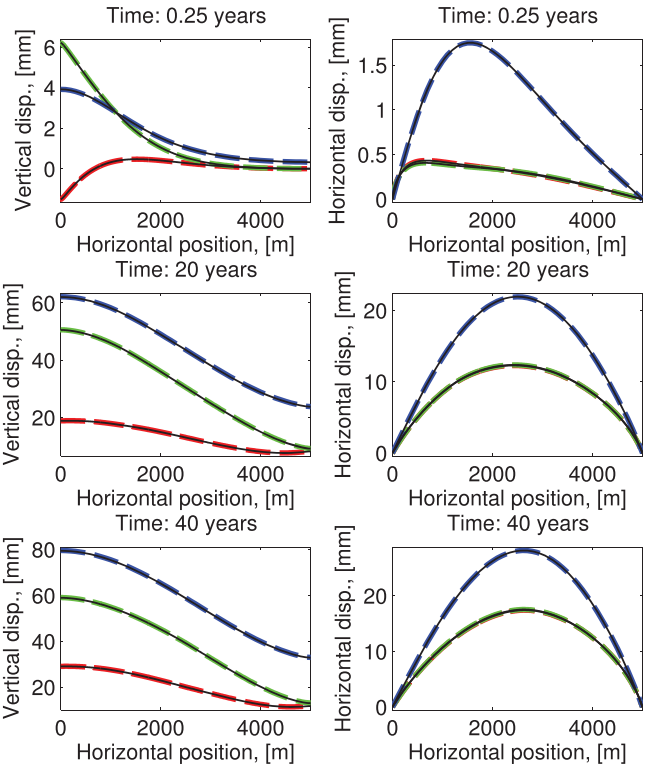

Figure 10. Plots of (left) vertical displacement and (right) horizontal displacement of the bottom and top of the aquifer and the model surface for three different times. Blue curves are at the surface of the model, green curves are at the top of aquifer and red curves are at the bottom of aquifer. Dashed lines are the solution from the fully resolved model and thin black lines are from the dimensionally reduced model. Note that in the figures to the right the horizontal displacement at the top and bottom of the aquifer (green and red curve, respectively) are almost the same and the two curves coincide.

of freedom that can be eliminated increases, see for example point B in Figure 12. The corresponding ratio of the simulation times is also shown in Figure 12 (left, blue line), and even if the reduction in degrees of freedom is modest, the reduction in calculation time becomes increasingly more significant.

In order to quantify the applicability of the dimensionally reduced model, a numerical convergence study was performed. *Yortsos* [1995] examined the validity of the VE assumption and identified the key dimensionless variable to be R_L defined as

$$R_L = \frac{L}{H}\sqrt{\frac{k_v}{k_h}} \tag{40}$$

where L is a characteristic length and k_v and k_h (m^2) are the vertical and horizontal permeability in the aquifer, respectively. The analysis showed that VE is valid in the limit of large R_L^2. In the validation model, the ratio $k_v/k_h = 1$, thus $R_L = L/H$ and the numerical convergence study is with respect to the thickness of the aquifer. The model setup was identical to the validation case, but in order to make sure that the injected CO_2 did not reach the outer boundary of the model, the injection rate was scaled with the thickness. The test was also done without any residual saturation of either phases. The large range of aquifer thickness (H varied from 2 to 100 m) required some special attention to the grid resolution in the aquifer, both in the lateral and vertical direction, to resolve the phase distribution. This affects the number of degrees of freedom in the aquifer that can be eliminated. The ratio of the computational cost (degrees of freedom) and the calculation time for the full-dimensional model versus the dimensionally reduced model for the various thicknesses are shown in Figure 12 (right).

As can be seen in both the time varying performance test of the validation model and the applicability test (convergence study) of varying aquifer thickness, Figure 12 (left and right, respectively), there are moderate

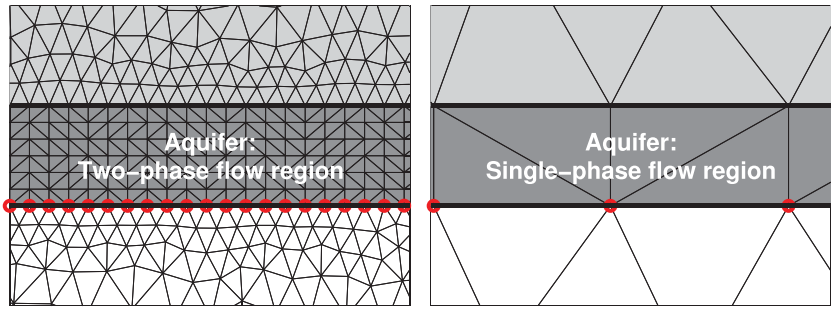

Figure 11. Example of the numerical grid in the aquifer. (left) Dense discretization in the two-phase flow region. (right) Coarse discretization in the single-phase flow region.

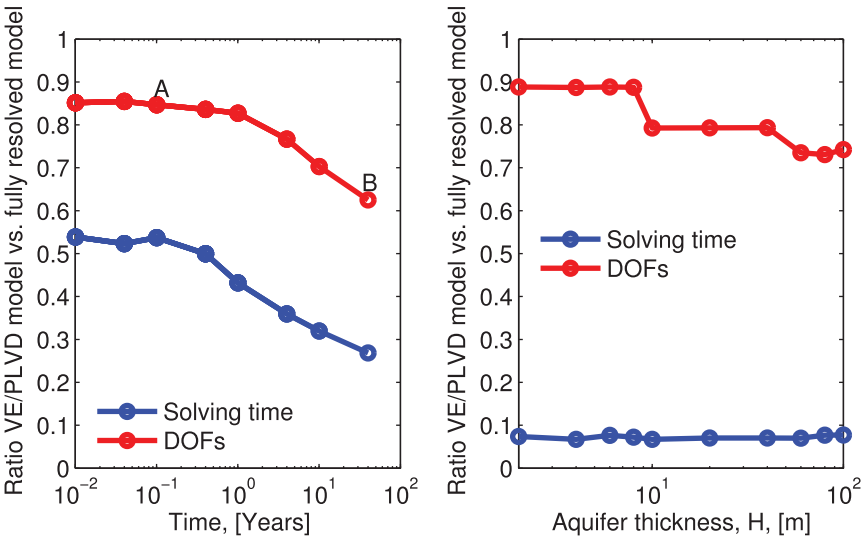

Figure 12. The ratio of numerical solving time and number of degrees of freedom (left) for various simulations times in the performance test, see text for description, and (right) for various aquifer thickness *H* after 20 years of injection in the convergence test.

reductions in cost, but the savings in calculation time by using the dimensionally reduced model are significant. As described earlier, this is partly the result of solving a reduced mathematical problem, but also, and more importantly, the result of solving a less stiff nonlinear system of equations in the dimensionally reduced model that allows for larger time steps by the numerical solver.

The main difference between the validation model and the convergence model is that in the latter the injection rate is scaled to the thickness and is also comparably higher (for $H = 20$ m it is 2.7 times higher, note that no residual saturation gives the injected CO_2 more pore volume to sweep across). Higher injection rates imply sharper saturation fronts, thus the applicability test further underlines the computational benefit of the dimensionally reduced form, namely that the system of equations is more efficient to solve.

5.2. Convergence

In the extreme case of a zero-thickness aquifer, the integrated equations reduce to continuity requirements on a surface, and thus the integrated model is exactly equivalent to the original full-dimensional equations. We thus expect that any modeling error will be a function of the aquifer thickness [*Yortsos*, 1995], see also equation (40). Since we are using a model with linear displacement, it is reasonable to expect the LVD model to be second-order accurate with respect to the aquifer thickness. However, due to the constant vertical potential used in the flow model, we expect the pressure to be only first-order accurate, which may impact the overall accuracy of the model. In practice, we may expect that the model accuracy lies somewhere between first and second order. We note that simpler models, with e.g., constant displacement across the aquifer thickness, are expected to be strictly less accurate. Unfortunately, a rigorous analysis of these statements is beyond the scope of this work, due to the nonlinearities present in the system, and we will therefore proceed with a purely numerical analysis of the model error as it depends on the aquifer thickness and consequently look closer at the results of the convergence study described in section 5.1.

Because analytical solutions for this problem is unavailable, we consider the full-dimensional simulation as the true model and measure the error as the relative difference in the solution obtained by the dimensionally reduced model and the fully resolved model. Furthermore, we measure the error in discrete points of interest, rather than using a spatial norm, in order to capture the accuracy exactly near the model reduction. The results are shown in Figure 13.

We note that in general a convergence between first and second order is obtained. We also remark that in all cases, the difference is small, with less than 1% in almost all cases considered. A notable feature in the convergence study is the irregularity of the plot. This stems from two cases: first, the full-dimensional grid has to be adapted to the thickness of the aquifer, and the gridding of the full model thus changes between

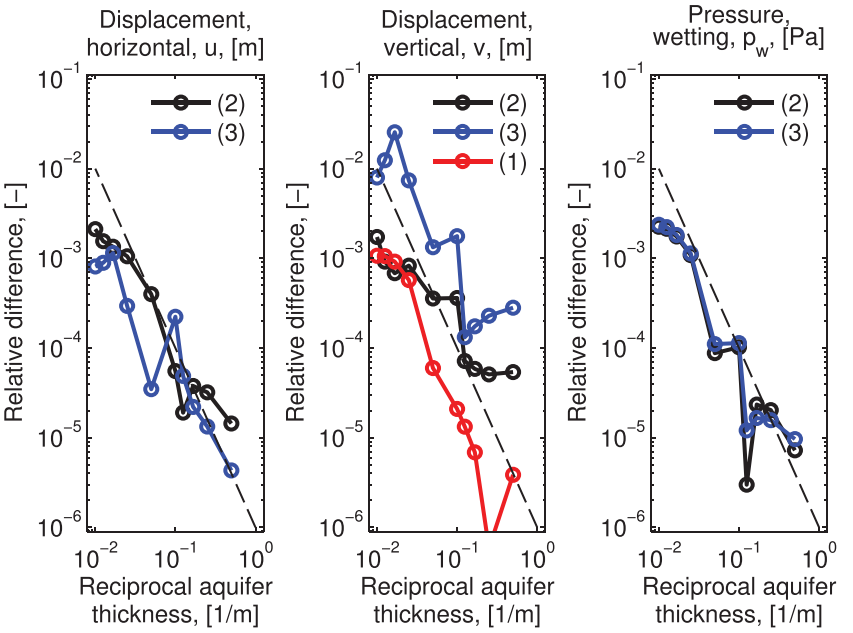

Figure 13. Convergence plot of the reciprocal of aquifer thickness *H* in various positions (position (1)–(3), as indicated in Figure 4). The thin, black dashed lines indicate second-order convergence. Thickness *H* varies from 2 to 100 m. The results are after 1 year of injection.

each case considered. Furthermore, for thin aquifers, the error is approaching the order of the tolerance of the nonlinear solver, and thus cannot be further reduced within the comparison paradigm chosen.

In sum, the convergence study indicates that the dimensionally reduced model has high accuracy for even relatively thick aquifers, and essentially second-order convergence properties compared to the fully resolved model with respect to aquifer thickness.

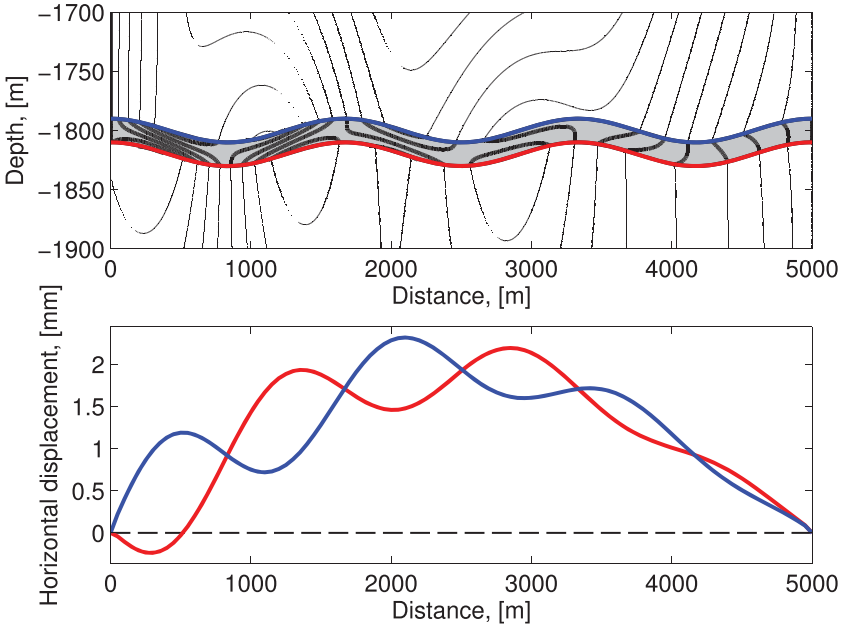

Figure 14. (top) Contours of the horizontal displacement in and around a topographic aquifer (grey, shaded area). Note the difference in scale. The overburden and underburden are assumed impermeable and a static pore pressure increase is applied to the aquifer that varies linearly from 15 MPa at the left boundary to zero at the right boundary. (bottom) Horizontal displacement along the top (blue line) and bottom (red line) surfaces of the aquifer.

5.3. Effect of Topography

As described in section 3.3.3, the assumption for the LVD and PLVD equations is linearly varying displacements across the thickness of the aquifer, see equation (33). In the validation model presented in section 4, it can be seen from the results that the horizontal displacement at the top and bottom of the aquifer is almost identical, see Figure 10 (right, green and red curves, respectively), making the assumption of constant horizontal displacement across the aquifer a good approximation. However, this is because the aquifer is flat and that the surrounding formations have the same mechanical properties. When the aquifer top and bottom topographies are variable, see example in Figure 14 (top), it can be clearly seen that there may be significant quantitative and qualitative differences in horizontal displacement across the aquifer. In this example, a 20 m thick reservoir varies sinusoidally of ± 10 m in the vertical direction. The mechanical properties are the same as in the validation model, see Table 1, but the overburden and underburden are now assumed impermeable and a static pore pressure change is applied to the aquifer that varies linearly from 15 MPa at the left boundary to zero (initial pore pressure p_0) at the right boundary. It can be seen from the horizontal displacement in Figure 14 (bottom) that it is far from constant across the aquifer, and at $x < 500$ m it even has opposite sign. This can be significant when considering the integrity of a caprock in CO_2 storage.

6. Conclusion

We have derived a reduced-dimensional model for coupled two-phase flow and geomechanical deformation within the context of CO_2 storage. The reduced-order model simplifies the complex flow and interaction within thin storage units, while retaining the full-dimensional poroelastic equations for the overburden and underburden.

Our presentation provides a general framework for reduced models; however, we emphasize our choices of closure relationship: Vertical Equilibrium (VE) for the fluid and Linear Vertical Deflection (LVD) for the solid within the aquifer. These choices allow for an efficient reconstruction of fluid saturation as well as realistic approximation of aquifer deformation, even in the presence of variable aquifer topography.

The current presentation is within the context of immiscible fluids, which couples the main fluid-mechanical coupling. We envision that recent work on advanced models for vertically integrated models for more complex processes, including fluid miscibility and accounting for vertical variation in fluid density, can be integrated with the current results. These coupled processes are important in that they are computationally demanding, and that simplified models are imperative to become computationally tractable.

In this study, the simplified model approach through dimensional reduction has proved promising in providing significant savings in computational time when faced with a large number of simulations. In general, a reduction in computational cost allows for faster calculation. However, it has been shown in both the validation model and a convergence study, see Figure 12 (left and right, respectively), that in addition to a reduction in cost, albeit modest, the dimensionally reduced formulation produces less stiff nonlinear systems of equations, allowing the numerical solver to progress with larger time steps and significantly contribute to further reduce the computational time.

It has also been demonstrated that such models can retain reasonable accuracy when applied to realistic field data, such as the conditions at CO_2 storage plant in In Salah, Algeria. The range of applicability of the dimensionally reduced model is to a leading order the thickness of the reduced domain, the aquifer. A convergence test for a range of aquifer thickness values indicates that accurate solutions in the order of 0.1% and less difference in solution compared to a full-dimensional formulation for aquifers up to 100 m thick are achieved.

The main parameter affecting the effective stress is the pore pressure that in this example is little affected by the phase distribution, hence the early-times violation of negligible vertical flow, the Vertical Equilibrium (VE) assumption, does not affect the stress. In a different scenario, for instance at lower depths where the density difference between the phases is bigger compared to the present scenario and the capillary pressure will have a bigger impact on the pore pressure, the accuracy will depend more on the validity of the Vertical Equilibrium assumption, and this has been investigated by others, see e.g., *Court et al*. [2012].

However, as illustrated here, the VE assumption becomes increasingly appropriate with time and is almost always appropriate for analysis of long-term behavior that can span many hundreds to thousands of years.

Appendix A

As the fluid phase pressures p_α can be expressed as a function of the vertical position z, so can the capillary pressure, $p_c(z)$. The average saturation S_α in equation (24) is the integral of the reconstructed inverted capillary saturation, $\hat{s}_\alpha$, which is derived from the inverted capillary pressure function $p_c^{-1}(z)$. From *Nordbotten and Dahle* [2010], we have that the reconstructed effective inverted capillary saturation for the nonwetting phase, $\hat{s}_{en}$, can be expressed by

$$\hat{s}_{en}(P_*^{cap}) = \begin{cases} 0, & 0 \le \zeta \\ 1 - \dfrac{1}{B^2\left(P_*^{cap} + \dfrac{z-\zeta_p}{H}\right)^2}, & \zeta < z \le H \end{cases} \tag{A1}$$

where B and P_*^{cap} are dimensionless constants [see *Nordbotten and Dahle*, 2010, for details], ζ (m) is the vertical location of the interface where $\hat{s}_{en}=0$, and $\hat{s}_{en}$ is related to $\hat{s}_n$ as in equation (37).

The expressions for the average phase mobilities can for simple constitutive functions (e.g., equations (38) and (39)) be calculated explicitly as

$$\Lambda_n(S_n) = \begin{cases} [Q(u_1,p) - Q(u_2,p)], & \zeta = 0 \\ [Q(u_1,p) - Q(1,p)], & \zeta > 0 \end{cases} \tag{A2}$$

and

$$\Lambda_w(S_n) = \begin{cases} \displaystyle\sum_{i=0}^{q} \binom{q}{i} (-1)^i [Q(u_1,i) - Q(u_2,i)], & \zeta = 0, \\ \displaystyle\sum_{i=0}^{q} \binom{q}{i} (-1)^i [Q(u_1,i) - Q(1,i)] + \dfrac{\zeta}{H}, & \zeta > 0. \end{cases} \tag{A3}$$

where

$$u_1 = BP_*^{cap} + B, \quad u_2 = BP_*^{cap} \tag{A4}$$

$$Q(u,p) = \frac{1}{B}\sum_{i=0}^{p} \binom{p}{i} \frac{(-1)^i}{1-2i} u^{1-2i} \tag{A5}$$

$$Q(u,q) = \frac{1}{B}\sum_{i=0}^{q} \binom{q}{i} \frac{(-1)^i}{1-2i} u^{1-2i} \tag{A6}$$

Acknowledgments
The authors are thankful to the following sponsors for the financial support of this work: Research Council of Norway (through the MatMoRA-II project 215641, Mathematical Modeling and Risk Assessment of CO_2 storage) and Statoil ASA and NGI in Oslo, Norway. Data used in this paper are properly cited and referred to in the reference list.

References

Andersen, O., S. E. Gasda, and H. M. Nilsen (2014), Vertically averaged equations with variable density for CO_2 flow in porous media, *Transp. Porous Media*, *107*, 1–33.
Bear, J., and M. Y. Corapcioglu (1981a), Mathematical model for regional land subsidence due to pumping: 1. Integrated aquifer subsidence equations based on vertical displacement only, *Water Resour. Res.*, *17*(4), 937–946.
Bear, J., and M. Y. Corapcioglu (1981b), Mathematical model for regional land subsidence due to pumping: 2. Integrated aquifer subsidence equations for vertical and horizontal displacements, *Water Resour. Res.*, *17*(4), 947–958.
Biot, M. A. (1935), Le problème de la consolidation de matières argileuses sous une charge, *Ann. Soc. Sci. Bruxelles, Ser. B*, *55*, 110–113.
Biot, M. A. (1941), General theory of three-dimensional consolidation, *J. Appl. Phys.*, *12*(2), 155–164.
Biot, M. A. (1955), Theory of elasticity and consolidation for a porous anisotropic solid, *J. Appl. Phys.*, *26*, 182–185.
Biot, M. A. (1972), Theory of finite deformations of porous solids, *Indiana Univ. Math. J.*, *21*, 597–620.
Biot, M. A. (1973), Nonlinear and semilinear rheology of porous solids, *J. Geophys. Res.*, 23, 4924–4937.
Bishop, A. W. (1959), The principle of effective stress, *Tek. Ukeblad*, *39*, 859–863.
Brooks, R. H., and A. T. Corey (1964), Hydraulic properties of porous media, *Hydrol. Pap. 3*, Colo. State Univ., Fort Collins.
Celia, M. A., and J. M. Nordbotten (2009), Practical modeling approaches for geological storage of carbon dioxide, *Ground Water*, *47*(5), 627–638, doi:10.1111/j.1745-6584.2009.00590.x.

Celia, M. A., J. M. Nordbotten, B. Court, M. Dobossy, and S. Bachu (2011), Field-scale application of a semi-analytical model for estimation of CO_2 and brine leakage along old wells, *Int. J. Greenhouse Gas Control*, *5*(2), 257–269, doi:10.1016/j.ijggc.2010.10.005.

Celia, M. A., S. Bachu, J. M. Nordbotten, and K. Bandilla (2015), Status of CO_2 storage in deep saline aquifers with emphasis on modeling approaches and practical simulations, *Water Resour. Res.*, *51*, 6846–6892, doi:10.1002/2015WR017609.

Class, H., et al. (2009), A benchmark study on problems related to CO_2 storage in geologic formations, *Comput. Geosci.*, *13*(4), 409–434, doi:10.1007/s10596-009-9146-x.

Corapcioglu, M. Y., and J. Bear (1983), A mathematical model for regional land subsidence due to pumping: 3. Integrated equations for a phreatic aquifer, *Water Resour. Res.*, *19*(4), 895–908.

Court, B., K. W. Bandilla, M. A. Celia, A. Janzen, M. Dobossy, and J. M. Nordbotten (2012), Applicability of vertical-equilibrium and sharp-interface assumptions in CO_2 sequestration modeling, *Int. J. Greenhouse Gas Control*, *10*, 134–147, doi:10.1016/j.ijggc.2012.04.015.

Deflandre, J.-P., A. Estublier, A. Baroni, J.-M. Daniel, and F. Adjémian (2011), In Salah CO_2 injection modeling: A preliminary approach to predict short term reservoir behavior, *Energy Procedia*, *4*, 3574–3581, doi:10.1016/j.egypro.2011.02.286.

Doster, F., J. M. Nordbotten, and M. A. Celia (2013), Impact of capillary hysteresis and trapping on vertically integrated models for CO_2 storage, *Adv. Water Resour.*, *62*, Part C, 465–474, doi:10.1016/j.advwatres.2013.09.005.

Durucan, S., J.-Q. Shi, C. Sinayuc, and A. Korre (2011), In Salah CO_2 storage JIP: Carbon dioxide plume extension around KB-502 well—New insights into reservoir behaviour at the In Salah storage site, *Energy Procedia*, *4*, 3379–3385, doi:10.1016/j.egypro.2011.02.260.

Elenius, M., D. Voskov, and H. Tchelepi (2015), Interactions between gravity currents and convective dissolution, *Adv. Water Resour.*, *83*, 77–88, doi:10.1016/j.advwatres.2015.05.006.

Ferrín, J. L., and A. Mikelić (2003), Homogenizing the acoustic properties of a porous matrix containing an incompressible inviscid fluid, *Math. Methods Appl. Sci.*, *26*(10), 831–859, doi:10.1002/mma.398.

Gasda, S. E., J. M. Nordbotten, and M. A. Celia (2011), Vertically averaged approaches for CO_2 migration with solubility trapping, *Water Resour. Res.*, *47*, W05528, doi:10.1029/2010WR009075.

Gemmer, L., O. Hansen, M. Iding, S. Leary, and P. Ringrose (2012), Geomechanical response to CO_2 injection at Krechba, In Salah, Algeria, *First Break*, *30*(2), 79–84.

Gor, G. Y., T. R. Elliot, and J. H. Prévost (2013), Effects of thermal stresses on caprock integrity during CO_2 storage, *Int. J. Greenhouse Gas Control*, *12*, 300–309, doi:10.1016/j.ijggc.2012.11.020.

Guo, B., K. W. Bandilla, F. Doster, E. Keilegavlen, and M. A. Celia (2014), A vertically integrated model with vertical dynamics for CO_2 storage, *Water Resour. Res.*, *50*(8), 6269–6284, doi:10.1002/2013WR015215.

Helmig, R. (1997), *Multiphase Flow and Transport Processes in the Subsurface: A Contribution to the Modeling of Hydrosystems*, Environ. Eng., Springer, Berlin.

Hesse, M. A., F. M. Orr, and H. A. Tchelepi (2008), Gravity currents with residual trapping, *J. Fluid Mech.*, *611*, 35–60.

Hunt, B. (1985), Flow to a well in a multiaquifer system, *Water Resour. Res.*, *21*(11), 1637–1641, doi:10.1029/WR021i011p01637.

Jaeger, J. C., N. G. W. Cook, and R. Zimmermann (2007), *Fundamentals of Rock Mechanics*, 4th ed., Wiley-Blackwell, Malden, Mass.

Lake, L. W. (1989), *Enhanced Oil Recovery*, Prentice Hall, Englewood Cliffs, N. J.

Lewis, R. W., and B. A. Schrefler (1998), *The Finite Element Method in the Static and Dynamic Deformation and Consolidation of Porous Media, Wiley Ser. Numer. Methods Eng.*, 2nd ed., John Wiley, N. Y.

Lide, D. R. (Ed.) (2003), *CRC Handbook of Chemistry and Physics*, 84th ed., CRC Press, Boca Raton, Fla.

Linstrom, P., and W. Mallard (Eds.) (2015), *NIST Chemistry WebBook, NIST Standard Reference Database Number 69*, Natl. Inst. of Stand. and Technol., Gaithersburg, Md.

Morris, J. P., Y. Hao, W. Foxall, and W. McNab (2011), A study of injection-induced mechanical deformation at the In Salah CO_2 storage project, *Int. J. Greenhouse Gas Control*, *5*(2), 270–280, doi:10.1016/j.ijggc.2010.10.004.

Mykkeltvedt, T. S., and J. M. Nordbotten (2012), Estimating convective mixing rates from commercial-scale CO_2 injection, *Environ. Earth Sci.*, *67*(2), 527–535, doi:10.1007/s12665-012-1674-3.

Nilsen, H. M., P. A. Herrera, M. Ashraf, I. Ligaarden, M. Iding, C. Hermanrud, K.-A. Lie, J. M. Nordbotten, H. K. Dahle, and E. Keilegavlen (2011), Field-case simulation of CO_2-plume migration using vertical-equilibrium models, *Energy Procedia*, *4*, 3801–3808, doi:10.1016/j.egypro.2011.02.315.

Nordbotten, J. M., and M. A. Celia (2006), An improved analytical solution for interface upconing around a well, *Water Resour. Res.*, *42*, W08433, doi:10.1029/2005WR004738.

Nordbotten, J. M., and M. A. Celia (2012), *Geological Storage of CO2: Modeling Approaches for Large-Scale Simulation*, 256 pp., John Wiley, Hoboken, N. J.

Nordbotten, J. M., and H. K. Dahle (2010), Impact of capillary forces on large-scale migration of CO_2, in *XVIII International Conference on Water Resources, CMWR 2010*, edited by J. Carrera, CIMNE, Barcelona, Spain.

Nordbotten, J. M., and H. K. Dahle (2011), Impact of the capillary fringe in vertically integrated models for CO_2 storage, *Water Resour. Res.*, *47*, W02537, doi:10.1029/2009WR008958.

Nordbotten, J. M., M. A. Celia, S. Bachu, and H. K. Dahle (2005), Semianalytical solution for CO_2 leakage through an abandoned well, *Environ. Sci. Technol.*, *39*(2), 602–611, doi:10.1021/es035338i.

Nordbotten, J. M., et al. (2012), Uncertainties in practical simulation of CO_2 storage, *Int. J. Greenhouse Gas Control*, *9*, 234–242, doi:10.1016/j.ijggc.2012.03.007.

Preisig, M., and J. H. Prévost (2011), Coupled multi-phase thermo-poromechanical effects. Case study: CO_2 injection at In Salah, Algeria, *Int. J. Greenhouse Gas Control*, *5*(4), 1055–1064, doi:10.1016/j.ijggc.2010.12.006.

Rice, J. R., and M. P. Cleary (1976), Some basic stress diffusion solutions for fluid-saturated elastic porous media with compressible constituents, *Rev. Geophys.*, *14*(2), 227–241.

Rinaldi, A. P., and J. Rutqvist (2013), Modeling of deep fracture zone opening and transient ground surface uplift at KB-502 CO_2 injection well, In Salah, Algeria, *Int. J. Greenhouse Gas Control*, *12*, 155–167, doi:10.1016/j.ijggc.2012.10.017.

Ringrose, P., A. Mathieson, I. Wright, F. Selama, O. Hansen, R. Bissell, N. Saoula, and J. Midgley (2013), The In Salah CO_2 storage project: Lessons learned and knowledge transfer, *Energy Procedia*, *37*, 6226–6236, doi:10.1016/j.egypro.2013.06.551.

Rutqvist, J., and O. Stephansson (2003), The role of hydromechanical coupling in fractured rock engineering, *Hydrogeol. J.*, *11*(1), 7–40.

Rutqvist, J., D. W. Vasco, and L. Myer (2010), Coupled reservoir-geomechanical analysis of CO_2 injection and ground deformations at In Salah, Algeria, *Int. J. Greenhouse Gas Control*, *4*(2), 225–230, doi:10.1016/j.ijggc.2009.10.017.

Shi, J.-Q., C. Sinayuc, S. Durucan, and A. Korre (2012), Assessment of carbon dioxide plume behaviour within the storage reservoir and the lower caprock around the KB-502 injection well at In Salah, *Int. J. Greenhouse Gas Control*, *7*, 115–126, doi:10.1016/j.ijggc.2012.01.002.

Vasco, D. W., A. Ferretti, and F. Novali (2008), Reservoir monitoring and characterization using satellite geodetic data: Interferometric synthetic aperture radar observations from the Krechba field, Algeria, *Geophysics*, *73*(6), WA113–WA122, doi:10.1190/1.2981184.

Wang, H. F. (2000), *Theory of Linear Poroelasticity With Applications to Geomechanics and Hydrology*, Princeton Univ. Press, Princeton, N. J.

Yan, W., S. Huang, and E. H. Stenby (2011), Measurement and modeling of CO_2 solubility in NaCl brine and CO_2 saturated NaCl brine density, *Int. J. Greenhouse Gas Control*, *5*(6), 1460–1477, doi:10.1016/j.ijggc.2011.08.004.

Yortsos, Y. C. (1995), A theoretical analysis of vertical flow equilibrium, *Transp. Porous Media*, *18*(2), 107–129, doi:10.1007/BF01064674.